

RESEARCH ARTICLE | JANUARY 10 2023

## Efficient implementation of time-dependent auxiliary density functional theory

Luis I. Hernández-Segura  ; Andreas M. Köster  



*J. Chem. Phys.*, 158, 024108 (2023)  
<https://doi.org/10.1063/5.0135263>



### Articles You May Be Interested In

Analytic second derivatives from auxiliary density perturbation theory

*J. Chem. Phys.* (December 2016)

Time-dependent auxiliary density perturbation theory

*J. Chem. Phys.* (August 2010)

Auxiliary density perturbation theory

*J. Chem. Phys.* (April 2008)



The Journal of Chemical Physics  
**Special Topics Open  
for Submissions**

[Learn More](#)

 AIP  
Publishing

# Efficient implementation of time-dependent auxiliary density functional theory

Cite as: J. Chem. Phys. 158, 024108 (2023); doi: 10.1063/5.0135263

Submitted: 17 November 2022 • Accepted: 19 December 2022 •

Published Online: 10 January 2023



View Online



Export Citation



CrossMark

Luis I. Hernández-Segura and Andreas M. Köster<sup>a)</sup>

## AFFILIATIONS

Departamento de Química, Cinvestav, Avenida Instituto Politécnico Nacional 2508, A.P. 14-740, CDMX C.P. 07360, Mexico

<sup>a)</sup>Author to whom correspondence should be addressed: akoster@cinvestav.mx

## ABSTRACT

The random phase approximation of time-dependent auxiliary density functional theory (TDADFT) is rederived from auxiliary density perturbation theory. Our exhaustive validation of TDADFT reveals an upshift of the excitation energies by ~0.1 eV with respect to standard time-dependent density functional theory. For the computationally efficient implementation of TDADFT, floating point operation optimized three-center electron repulsion integral recurrence relations and their double asymptotic expansions are implemented into the Davidson solver. The computational efficiency of TDADFT is benchmarked with four sets of molecules comprising alkanes, fullerenes, DNA fragments, and zeolites. The results show that TDADFT has a computational scaling between 1.3 and 1.9 with respect to the number of basis functions, which is lower than the scaling of standard time-dependent density functional theory. Due to its computational simplifications, TDADFT is particularly well suited for Born-Oppenheimer molecular dynamics simulations. As illustrative examples, we present the temperature effects on the gas-phase absorption spectra of benzene, naphthalene, and anthracene.

Published under an exclusive license by AIP Publishing. <https://doi.org/10.1063/5.0135263>

## I. INTRODUCTION

One of the most popular methods for calculating excited state properties is linear response time-dependent density functional theory (TDDFT). The applicability of this method ranges from the calculation of excitation energies,<sup>1</sup> absorption spectra,<sup>2</sup> polarizabilities<sup>3</sup> and energy gradients<sup>4</sup> of excited states to the optimization of conical intersections<sup>5,6</sup> and avoided-crossings<sup>7</sup> between potential energy surfaces of different electronic states. Recent developments in femtosecond transient absorption spectroscopy have permitted to obtain experimental information on the absorption and emission spectra of molecules a few femtoseconds after the initial electronic excitation.<sup>8</sup> Using this experimental information together with theoretical calculations, it is now possible to determine if the molecule relaxes the energy through light emission, energy surface crossing that can lead to Stoke shifts, stimulated emission, and fluorescence or promotes into an intramolecular charge transfer state. Although TDDFT is nowadays widely used, it is not free of drawbacks. By construction, TDDFT fails to describe states with double excitations.<sup>9,10</sup> This type of excitations can become relevant near conical intersections, potential energy surface crossings, or charge transfer states. Thus, failures of TDDFT for these situations must be anticipated. Another drawback of TDDFT is the underestimation, up to several electron volts, of excitation energies to Rydberg states.<sup>11</sup> Large errors

also plague charge transfer (CT) excitations, where the accuracy is not even qualitative when using “pure” exchange-correlation functionals,<sup>12,13</sup> i.e., the local density (LDA) or generalized gradient (GGA) approximation.

Despite these downsides, the advantages of TDDFT predominate. These are (i) The accuracy, of ~0.3 eV when describing valence excited states. This accuracy competes well with sophisticated wave function methods such as equation of motion coupled cluster theory with singles and doubles (EOM-CCSD), configuration interaction theory with singles and doubles, CIS(D), and Belthe-Salpeter equation based on GW quasiparticle energies (BSE@GW).<sup>14,15</sup> (ii) The fact that the user has not to provide insight knowledge of the system under consideration. This is an important difference to, for example, CASPT2 where the selection of the active space requires system specific chemical insight of the molecules studied. In order to perform a TDDFT calculation the only insight needed, as with DFT, is a suitable exchange-correlation functional and basis set, for which there are several published reference works.<sup>2,15–19</sup> Thus, TDDFT is well suited for the qualitative exploration of excited states and excited potential energy surfaces in new and complex molecular systems. (iii) The low computational scaling that matches that of BSE@GW<sup>14</sup> and outperforms all other available methods. Here, we show that a further reduction of the formal scaling of TDDFT is possible within the framework of auxiliary density functional

theory (ADFT). This further improvement in the computational performance is achieved by the use of the auxiliary density from the variational fitting of the Coulomb potential for the calculation of the exchange-correlation potential and kernel.<sup>20</sup> We name the resulting approach time-dependent ADFT (TDADFT). In previous TDADFT implementations, the three-center electron repulsion integrals were either read from tape (Conventional)<sup>20</sup> or calculated on-the-fly (Direct)<sup>21,22</sup> by corresponding integral recurrence relations. In particular, no advantage was taken from the double asymptotic three-center electron repulsion integral (ERI) expansion,<sup>23</sup> which is critical for low-order scaling in large molecular ADFT calculations. Our new implementation overcomes this drawback. It permits the combination of on-the-fly near field ERI calculation with the double asymptotic expansion for far field ERIs as well as the extension of the Mixed self-consistent field (SCF) methodology to TDADFT calculations. In this approach, near field three-center ERIs are stored in random access memory (RAM), whereas far field ERIs are calculated on-the-fly using the double asymptotic expansion. Moreover, in our new implementation, the minimal residue (MINRES) method, which avoids the inversion of the two-center ERI matrix,<sup>24</sup> is now available for the solution of density fitting analog equation systems in TDADFT.

The purpose of this paper is to demonstrate that TDADFT retains the accuracy of TDDFT, albeit with a significantly reduced computational demand. Because our implementation of TDADFT follows closely the well-established implementation of auxiliary density perturbation theory (ADPT),<sup>25</sup> we derive the random phase approximation (RPA) of TDADFT in the framework of time-dependent ADPT<sup>26</sup> in Sec. II. The implementation details and computational methodologies are described in Secs. III and IV, respectively. The results given in Sec. V are divided into three subsections that discuss our exhaustive validation of TDADFT, its performance analysis and Born–Oppenheimer molecular dynamics (BOMD) simulations that incorporate temperature and non-harmonic vibrational effects into UV–Vis absorption spectra of simple aromatics. Final conclusions are given in Sec. VI.

## II. THEORY

In time-dependent ADPT, the time dependency is introduced through an external oscillating electric field operator<sup>27</sup> added as a perturbation to the time-independent Kohn–Sham operator,  $\widehat{\mathbf{K}}$ ,

$$\widehat{\mathbf{K}}(t) = \widehat{\mathbf{K}} + \vec{\mathbf{E}} \cdot \vec{\mathbf{r}} (e^{-i\omega t} + e^{i\omega t}). \quad (1)$$

The resulting time-dependent Kohn–Sham equation can be expanded with respect to a perturbation parameter  $\lambda$ , which in our case is a component of the external oscillating electric field, around the initial state that is available from a self-consistent field (SCF) solution. Thus, the following commutator equations, assuming orthonormal atomic basis functions, apply,

$$0 = [\mathbf{K}, \mathbf{P}], \quad (2)$$

$$i \frac{\partial \mathbf{P}^{(\lambda)}(t)}{\partial t} = [\mathbf{K}, \mathbf{P}^{(\lambda)}(t)] + [\mathbf{K}^{(\lambda)}(t), \mathbf{P}]. \quad (3)$$

The continuous time-dependent Kohn–Sham commutator, Eq. (3), can be expressed in the frequency domain through a Fourier

transformation. This leads to two discrete commutator equations that depend on the frequency of the external oscillating electric field.<sup>26</sup> One for the positive and the other for the negative frequency,  $\omega$ , due to the time-reversibility of the time-dependent operator,

$$\pm \omega \mathbf{P}^{(\lambda)}(\pm \omega) = [\mathbf{K}, \mathbf{P}^{(\lambda)}(\pm \omega)] + [\mathbf{K}^{(\lambda)}(\pm \omega), \mathbf{P}]. \quad (4)$$

Here, the (closed-shell) perturbed density matrix,  $\mathbf{P}^{(\lambda)}(\pm \omega)$ , is defined in terms of the occupied perturbed and unperturbed molecular orbital (MO) coefficients<sup>28</sup> as

$$P_{\mu\nu}^{(\lambda)}(\pm \omega) = 2 \sum_i^{\text{occ}} c_{\mu i}^{(\lambda)}(\pm \omega) c_{\nu i} + 2 \sum_i^{\text{occ}} c_{\mu i} c_{\nu i}^{(\lambda)}(\mp \omega). \quad (5)$$

Note that  $P_{\mu\nu}^{(\lambda)}(\pm \omega)$  is not symmetric for  $\omega \neq 0$ ! However, the following relation holds for the perturbed density matrices,<sup>29</sup>

$$P_{\mu\nu}^{(\lambda)}(+\omega) = P_{\nu\mu}^{(\lambda)}(-\omega). \quad (6)$$

The perturbed MO coefficients for both  $+\omega$  and  $-\omega$  are given by

$$c_{\mu i}^{(\lambda)}(\pm \omega) = \sum_a^{\text{uno}} c_{\mu a} U_{ai}^{(\lambda)}(\pm \omega). \quad (7)$$

In Eq. (7), we use the conventional MO notation, namely  $i, j$  for canonical occupied (*occ*) MOs and  $a, b$  for canonical unoccupied (*uno*) MOs.

Once the perturbed density matrix is calculated, e.g., by time-dependent ADPT,<sup>26</sup> the dynamic polarizability tensor elements can be obtained through the following expectation value,

$$\alpha_{\kappa\lambda}(\omega) = - \sum_{\mu, \nu} P_{\mu\nu}^{(\lambda)}(+\omega) \langle \mu | r_\kappa | \nu \rangle. \quad (8)$$

In Eq. (8),  $\kappa$  and  $\lambda$  denote Cartesian components. Due to the symmetry of the dipole matrix elements and the relation in Eq. (6) for the perturbed density matrix elements, the dynamic polarizability tensor elements are identical for the  $+\omega$  and  $-\omega$  branches. Thus, the perturbed density  $P_{\mu\nu}^{(\lambda)}(+\omega)$  is chosen for the derivation in this work. Because TDADFT in its current form is restricted to LDA and GGA, the perturbed Kohn–Sham matrix is identical for  $+\omega$  and  $-\omega$ , which we indicate by an unsigned  $\omega$  dependency.

By introducing the molecular dipole matrix elements,

$$\Gamma_{ai}^{(\kappa)} = \sum_{\mu, \nu} c_{\mu i} c_{\nu a} \langle \mu | r_\kappa | \nu \rangle, \quad (9)$$

and expanding the perturbed density matrix elements in Eq. (8) according to Eqs. (5) and (7), the dynamic polarizability tensor elements can be expressed in terms of the MO transformation matrices,  $U_{ai}^{(\lambda)}(\pm \omega)$ , as

$$\alpha_{\kappa\lambda}(\omega) = -2 \sum_i^{\text{occ}} \sum_a^{\text{uno}} U_{ai}^{(\lambda)}(+\omega) \Gamma_{ai}^{(\kappa)} - 2 \sum_i^{\text{occ}} \sum_a^{\text{uno}} U_{ai}^{(\lambda)}(-\omega) \Gamma_{ai}^{(\kappa)}. \quad (10)$$

On the other hand, substituting Eqs. (5) and (7) into the commutator of Eq. (4) yields

$$\begin{aligned}
& 2\omega \sum_i^{\text{occ uno}} \sum_a c_{\mu a} U_{ai}^{(\lambda)}(+\omega) c_{vi} + 2\omega \sum_i^{\text{occ uno}} \sum_a c_{\mu i} U_{ai}^{(\lambda)}(-\omega) c_{va} \\
& = + 2 \sum_i^{\text{occ uno}} \sum_a \sum_{\sigma} K_{\mu\sigma} c_{\sigma a} U_{ai}^{(\lambda)}(+\omega) c_{vi} \\
& + 2 \sum_i^{\text{occ uno}} \sum_a \sum_{\sigma} K_{\mu\sigma} c_{\sigma i} U_{ai}^{(\lambda)}(-\omega) c_{va} \\
& - 2 \sum_i^{\text{occ uno}} \sum_a \sum_{\sigma} c_{\mu a} U_{ai}^{(\lambda)}(+\omega) c_{\sigma i} K_{\sigma v} \\
& - 2 \sum_i^{\text{occ uno}} \sum_a \sum_{\sigma} c_{\mu i} U_{ai}^{(\lambda)}(-\omega) c_{\sigma a} K_{\sigma v} \\
& + 2 \sum_i^{\text{occ}} \sum_{\sigma} K_{\mu\sigma}^{(\lambda)}(\omega) c_{\sigma i} c_{vi} - 2 \sum_i^{\text{occ}} \sum_{\sigma} c_{\mu i} c_{\sigma i} K_{\sigma v}^{(\lambda)}(\omega). \quad (11)
\end{aligned}$$

For convenience, we use an orthonormalized atomic basis such that  $\mathbf{c}^T \mathbf{c} = \mathbf{E}$  holds. Projection of Eq. (11) to MO space is achieved by multiplying from the left with  $c_{\mu p}$  and from the right with  $c_{vq}$ , where  $p$  and  $q$  refer to arbitrary MO indices. After summing over  $\mu$ ,  $v$  and  $\sigma$ , we obtain,

$$\begin{aligned}
& 2\omega \sum_i^{\text{occ uno}} \sum_a \delta_{pa} U_{ai}^{(\lambda)}(+\omega) \delta_{iq} + 2\omega \sum_i^{\text{occ uno}} \sum_a \delta_{pi} U_{ai}^{(\lambda)}(-\omega) \delta_{aq} \\
& = 2 \sum_i^{\text{occ uno}} \sum_a K_{pa} U_{ai}^{(\lambda)}(+\omega) \delta_{iq} + 2 \sum_i^{\text{occ uno}} \sum_a K_{pi} U_{ai}^{(\lambda)}(-\omega) \delta_{aq} \\
& - 2 \sum_i^{\text{occ uno}} \sum_a \delta_{pa} U_{ai}^{(\lambda)}(+\omega) K_{iq} - 2 \sum_i^{\text{occ uno}} \sum_a \delta_{pi} U_{ai}^{(\lambda)}(-\omega) K_{aq} \\
& + 2 \sum_i^{\text{occ}} K_{pi}^{(\lambda)}(\omega) \delta_{iq} - 2 \sum_i^{\text{occ}} \delta_{pi} K_{iq}^{(\lambda)}(\omega). \quad (12)
\end{aligned}$$

For  $p, q \in \text{occ}$  and  $p, q \in \text{uno}$ , Eq. (12) vanishes identically for a self-consistent field (SCF) solution. For  $p = b \in \text{uno} \wedge q = j \in \text{occ}$  follows from Eq. (12),

$$\omega U_{bj}^{(\lambda)}(+\omega) = \sum_a^{\text{uno}} K_{ba} U_{aj}^{(\lambda)}(+\omega) - \sum_i^{\text{occ}} U_{bi}^{(\lambda)}(+\omega) K_{ij} + K_{bj}^{(\lambda)}(\omega). \quad (13)$$

Similar, we find for  $p = j \in \text{occ} \wedge q = b \in \text{uno}$ ,

$$\omega U_{bj}^{(\lambda)}(-\omega) = \sum_i^{\text{occ}} U_{bi}^{(\lambda)}(-\omega) K_{ij} - \sum_a^{\text{uno}} K_{ba} U_{aj}^{(\lambda)}(-\omega) - K_{jb}^{(\lambda)}(\omega). \quad (14)$$

Exploiting the diagonal structure of the molecular Kohn–Sham matrices at SCF convergences, i.e.,  $K_{ij} = \epsilon_j \delta_{ij}$  and  $K_{ba} = \epsilon_b \delta_{ba}$ , we can write Eqs. (13) and (14) as

$$\epsilon_b U_{bj}^{(\lambda)}(+\omega) - \epsilon_j U_{bj}^{(\lambda)}(+\omega) - \omega U_{bj}^{(\lambda)}(+\omega) = -K_{bj}^{(\lambda)}(\omega), \quad (15)$$

$$\epsilon_b U_{bj}^{(\lambda)}(-\omega) - \epsilon_j U_{bj}^{(\lambda)}(-\omega) + \omega U_{bj}^{(\lambda)}(-\omega) = -K_{bj}^{(\lambda)}(\omega). \quad (16)$$

In Eq. (16),  $K_{ai}^{(\lambda)}(\omega) = K_{ia}^{(\lambda)}(\omega)$ , which holds when no Fock exchange is included, has been used. From Eqs. (15) and (16), the coupled perturbed Kohn–Sham (CPKS) linear equation systems for pure functionals<sup>28</sup> are obtained,

$$U_{ai}^{(\lambda)}(\pm\omega) = -\frac{K_{ai}^{(\lambda)}(\omega)}{\epsilon_a - \epsilon_i \mp \omega}. \quad (17)$$

The perturbed ADFT Kohn–Sham matrix  $K_{ai}^{(\lambda)}(\omega)$ , assuming perturbation independent basis and auxiliary functions, is given in LDA and GGA by

$$\begin{aligned}
K_{ai}^{(\lambda)}(\omega) &= \Gamma_{ai}^{(\lambda)} + 2 \sum_j^{\text{occ uno}} \sum_b \sum_{\bar{k}, \bar{l}} \langle ai \parallel \bar{k} \rangle O_{\bar{k} \bar{l}} \langle \bar{l} \parallel bj \rangle \\
&\times \left( U_{bj}^{(\lambda)}(+\omega) + U_{bj}^{(\lambda)}(-\omega) \right). \quad (18)
\end{aligned}$$

To ease notation, the following matrix elements were introduced,

$$O_{\bar{k} \bar{l}} = G_{\bar{k} \bar{l}}^{-1} + \sum_{\bar{m}, \bar{n}} G_{\bar{k} \bar{m}}^{-1} \langle \bar{m} | f_{xc}[\bar{\rho}] | \bar{n} \rangle G_{\bar{n} \bar{l}}^{-1}. \quad (19)$$

Introducing the explicit expressions of  $K_{ai}^{(\lambda)}(\omega)$ , Eq. (18), into the equation systems given by Eqs. (15) and (16) yields for  $\Gamma_{ai}^{(\lambda)}$ ,

$$\begin{aligned}
-\Gamma_{ai}^{(\lambda)} &= \sum_j^{\text{occ uno}} \sum_b \left[ (\epsilon_a - \epsilon_i) \delta_{ab} \delta_{ij} + 2 \sum_{\bar{k}, \bar{l}} \langle ai \parallel \bar{k} \rangle O_{\bar{k} \bar{l}} \langle \bar{l} \parallel bj \rangle \right] \\
&\times U_{bj}^{(\lambda)}(+\omega) + 2 \sum_j^{\text{occ uno}} \sum_b \sum_{\bar{k}, \bar{l}} \langle ai \parallel \bar{k} \rangle O_{\bar{k} \bar{l}} \langle \bar{l} \parallel bj \rangle \\
&\times U_{bj}^{(\lambda)}(-\omega) - \omega U_{ai}^{(\lambda)}(+\omega). \quad (20)
\end{aligned}$$

Similar, we find for  $\Gamma_{ia}^{(\lambda)}$ ,

$$\begin{aligned}
-\Gamma_{ia}^{(\lambda)} &= \sum_j^{\text{occ uno}} \sum_b \left[ (\epsilon_a - \epsilon_i) \delta_{ab} \delta_{ij} + 2 \sum_{\bar{k}, \bar{l}} \langle ai \parallel \bar{k} \rangle O_{\bar{k} \bar{l}} \langle \bar{l} \parallel bj \rangle \right] \\
&\times U_{bj}^{(\lambda)}(-\omega) + 2 \sum_j^{\text{occ uno}} \sum_b \sum_{\bar{k}, \bar{l}} \langle ai \parallel \bar{k} \rangle O_{\bar{k} \bar{l}} \langle \bar{l} \parallel bj \rangle \\
&\times U_{bj}^{(\lambda)}(+\omega) + \omega U_{ai}^{(\lambda)}(-\omega). \quad (21)
\end{aligned}$$

Equations (20) and (21) can be casted into the following equation system that relates the MO transformation matrices,  $\mathbf{U}^{(\lambda)}(\pm\omega)$ , with the dipole moment matrices,  $\mathbf{\Gamma}^{(\lambda)}$ ,

$$\begin{aligned}
-\begin{pmatrix} \Gamma_{ai}^{(\lambda)} \\ \Gamma_{ia}^{(\lambda)} \end{pmatrix} &= \sum_j^{\text{occ uno}} \sum_b \left[ \begin{pmatrix} A_{ai,bj} & B_{ai,bj} \\ B_{ai,bj} & A_{ai,bj} \end{pmatrix} \right. \\
&\left. - \omega \begin{pmatrix} \delta_{ab} \delta_{ij} & 0 \\ 0 & -\delta_{ab} \delta_{ij} \end{pmatrix} \right] \begin{pmatrix} U_{bj}^{(\lambda)}(+\omega) \\ U_{bj}^{(\lambda)}(-\omega) \end{pmatrix}. \quad (22)
\end{aligned}$$

The definitions of the (closed-shell)  $\mathbf{A}$  and  $\mathbf{B}$  super matrix elements for singlet excitations are given within ADFT<sup>21</sup> as

$$A_{ai,bj} = (\epsilon_a - \epsilon_i) \delta_{ab} \delta_{ij} + B_{ai,bj}, \quad (23)$$

$$B_{ai,bj} = 2 \sum_{\bar{k}, \bar{l}} \langle ai \parallel \bar{k} \rangle O_{\bar{k} \bar{l}} \langle \bar{l} \parallel bj \rangle. \quad (24)$$

These expressions confirm the recently discussed internal consistency of TDADFT by Mejia-Rodríguez and Trickey.<sup>30</sup> Solving Eq. (22) yields the MO transformation matrices, which in turn permits the calculation of the dynamical polarizability tensor elements according to Eq. (10). The dynamical polarizability,  $\alpha(\omega)$ , tends to  $\pm\infty$  at its poles that can be interpreted as excitations of the system. To obtain an equation system that calculates the values of  $\omega$  at which these poles of the dynamic polarizability are found, it is useful to write the perturbation matrix,  $\mathbf{U}^{(\lambda)}(\pm\omega)$ , in form of a magnitude,  $d_\lambda(\omega)$ , and a vector in the following way,

$$\begin{pmatrix} U_{bj}^{(\lambda)}(+\omega) \\ U_{bj}^{(\lambda)}(-\omega) \end{pmatrix} = d_\lambda(\omega) \begin{pmatrix} X_{bj}^{(\lambda)}(\omega) \\ Y_{bj}^{(\lambda)}(\omega) \end{pmatrix}. \quad (25)$$

According to Eq. (25) the change from the  $+\omega$  to the  $-\omega$  branch results on the right-hand side of this equation only in an interchange of the  $X_{bj}^{(\lambda)}(\omega)$  and  $Y_{bj}^{(\lambda)}(\omega)$  elements. To proceed, we now multiply Eq. (22) from the left by the row vector  $2(U_{ai}^{(\lambda)}(+\omega), U_{ai}^{(\lambda)}(-\omega))$ . This yields the diagonal dynamic polarizability tensor elements as defined by Eq. (10). By expressing the MO transformation matrix elements through Eq. (25), we obtain these tensor elements,

$$\begin{aligned} \alpha_{\lambda\lambda}(\omega) &= -2d_\lambda(\omega) \sum_i^{\text{occ}} \sum_a^{\text{uno}} (X_{ai}^{(\lambda)}(\omega) + Y_{ai}^{(\lambda)}(\omega)) \Gamma_{ai}^{(\lambda)} \\ &= 2d_\lambda^2(\omega) \sum_{i,j}^{\text{occ}} \sum_{a,b}^{\text{uno}} X_{ai}^{(\lambda)}(\omega) A_{ai,bj} X_{bj}^{(\lambda)}(\omega) \\ &\quad + 2d_\lambda^2(\omega) \sum_{i,j}^{\text{occ}} \sum_{a,b}^{\text{uno}} X_{ai}^{(\lambda)}(\omega) B_{ai,bj} Y_{bj}^{(\lambda)}(\omega) \\ &\quad + 2d_\lambda^2(\omega) \sum_{i,j}^{\text{occ}} \sum_{a,b}^{\text{uno}} Y_{ai}^{(\lambda)}(\omega) B_{ai,bj} X_{bj}^{(\lambda)}(\omega) \\ &\quad + 2d_\lambda^2(\omega) \sum_{i,j}^{\text{occ}} \sum_{a,b}^{\text{uno}} Y_{ai}^{(\lambda)}(\omega) A_{ai,bj} Y_{bj}^{(\lambda)}(\omega) \\ &\quad - 2d_\lambda^2(\omega) \omega \sum_i^{\text{occ}} \sum_a^{\text{uno}} (X_{ai}^{(\lambda)}(\omega) X_{ai}^{(\lambda)}(\omega) - Y_{ai}^{(\lambda)}(\omega) Y_{ai}^{(\lambda)}(\omega)). \end{aligned} \quad (26)$$

We now introduce, without loss of generality, the following normalization,

$$\sum_i^{\text{occ}} \sum_a^{\text{uno}} (X_{ai}^{(\lambda)}(\omega) X_{ai}^{(\lambda)}(\omega) - Y_{ai}^{(\lambda)}(\omega) Y_{ai}^{(\lambda)}(\omega)) \equiv 1. \quad (27)$$

To further ease notation, we also introduce,

$$p_\lambda(\omega) = \sum_i^{\text{occ}} \sum_a^{\text{uno}} X_{ai}^{(\lambda)}(\omega) \Gamma_{ai}^{(\lambda)} + \sum_i^{\text{occ}} \sum_a^{\text{uno}} Y_{ai}^{(\lambda)}(\omega) \Gamma_{ai}^{(\lambda)}, \quad (28)$$

$$\begin{aligned} q_{\lambda\lambda}(\omega) &= \sum_{i,j}^{\text{occ}} \sum_{a,b}^{\text{uno}} X_{ai}^{(\lambda)}(\omega) A_{ai,bj} X_{bj}^{(\lambda)}(\omega) \\ &\quad + \sum_{i,j}^{\text{occ}} \sum_{a,b}^{\text{uno}} X_{ai}^{(\lambda)}(\omega) B_{ai,bj} Y_{bj}^{(\lambda)}(\omega) \\ &\quad + \sum_{i,j}^{\text{occ}} \sum_{a,b}^{\text{uno}} Y_{ai}^{(\lambda)}(\omega) B_{ai,bj} X_{bj}^{(\lambda)}(\omega) \\ &\quad + \sum_{i,j}^{\text{occ}} \sum_{a,b}^{\text{uno}} Y_{ai}^{(\lambda)}(\omega) A_{ai,bj} Y_{bj}^{(\lambda)}(\omega) \end{aligned} \quad (29)$$

Therefore, we can rewrite Eq. (26) as

$$\alpha_{\lambda\lambda}(\omega) = -2d_\lambda(\omega)p_\lambda(\omega) = 2d_\lambda^2(\omega)(q_{\lambda\lambda}(\omega) - \omega). \quad (30)$$

Rearrangement of Eq. (30) yields

$$\alpha_{\lambda\lambda}(\omega) = \frac{2p_\lambda^2(\omega)}{q_{\lambda\lambda}(\omega) - \omega}. \quad (31)$$

Based on Eq. (31) a pole in the diagonal elements of the dynamic polarizability tensor appears if  $q_{\lambda\lambda}(\omega) - \omega = 0 \wedge p_\lambda \neq 0$  holds. Note that the condition  $p_\lambda \neq 0$  implies nonvanishing transition moments  $\Gamma_{ai}^{(\lambda)}$ . Expanding  $q_{\lambda\lambda}(\omega) - \omega = 0$  yields the so-called Casida equations<sup>31</sup> that were introduced as the random phase approximation (RPA) to TDDFT,

$$\begin{pmatrix} A & B \\ B & A \end{pmatrix} \begin{pmatrix} X \\ Y \end{pmatrix} = \omega \begin{pmatrix} 1 & -0 \\ 0 & -1 \end{pmatrix} \begin{pmatrix} X \\ Y \end{pmatrix} \quad (32)$$

Since the equation system no longer contains the dipole matrix elements,  $\Gamma_{ai}^{(\lambda)}$ , and the solutions are the same for  $\pm\omega$  the dependency on the sign of  $\omega$  and the perturbation parameter,  $\lambda$ , will be dropped from now on. This equation system can be reformulated in a smaller-dimension<sup>21</sup> by rewriting it into the following form:

$$AX + BY = \omega X, \quad (33)$$

$$BX + AY = -\omega Y. \quad (34)$$

The addition and subtraction of Eqs. (33) and (34) yields

$$(A + B)(X + Y) = \omega(X - Y), \quad (35)$$

$$(A - B)(X - Y) = \omega(X + Y). \quad (36)$$

Inserting Eq. (35) into Eq. (36) leads to

$$(A - B)(A + B)(X + Y) = \omega^2(X + Y). \quad (37)$$

The matrix  $(A - B)$  is diagonal when no Fock exchange is used as in the current work. In this case, Eq. (35) can be multiplied

from the left-hand side by  $(A - B)^{1/2}$  yielding the RPA TDADFT equation system,

$$\Omega F = \omega^2 F, \quad (38)$$

$$\Omega = (A - B)^{1/2} (A + B) (A - B)^{1/2}, \quad (39)$$

$$F = (A - B)^{-1/2} (X + Y). \quad (40)$$

By setting the  $B$  matrix equal to zero, the Tamm-Danoff approximation to TDDFT (TDA) is obtained,<sup>32</sup>

$$AX = \omega X. \quad (41)$$

In order to demonstrate the derived relationship between poles in the diagonal elements of the dynamical polarizability tensor and RPA TDADFT excitation energies, Eq. (31), we depict in Fig. 1 the average dynamical polarizability,

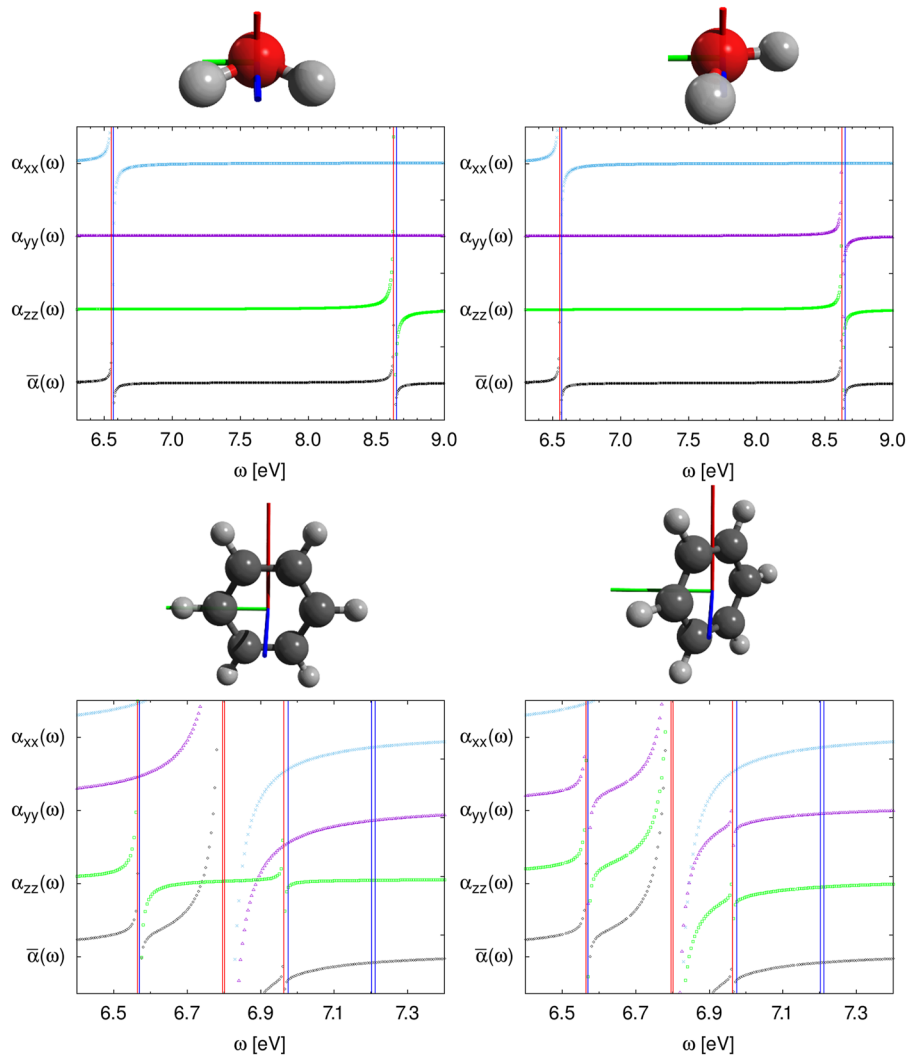


**FIG. 1.** Schematic plots of the average dynamical polarizabilities,  $\bar{\alpha}(\omega)$ , and corresponding tensor diagonal elements  $\alpha_{xx}$  (blue),  $\alpha_{yy}$  (purple) and  $\alpha_{zz}$  (green), for water (top) and benzene (bottom) as a function of  $\omega$  in the displayed molecular orientations. The RPA and TDA TDADFT excitation energies are depicted by red and blue vertical lines, respectively. The y-axis is scaled to aid visualization.

as a function of  $\omega$  along with the corresponding diagonal tensor elements for water and benzene in two different orientations. These orientations differ by a rotation of 45° around the (red)  $x$ -axis. The calculations were performed at the Vosko-Wilk-Nusair (VWN)<sup>33,34</sup>/aug-cc-pVTZ<sup>35</sup>/GEN-A2\*<sup>36</sup> level of theory. The depicted polarizabilities are scaled to obtain a better visualization. For comparison, the RPA (red) and TDA (blue) excitation energies with reasonable strong intensities are plotted as vertical lines, too. As this figure shows the poles of the polarizability tensor diagonal elements are not invariant with respect to the orientation of the molecule. Take as example the  $\alpha_{yy}(\omega)$  tensor component of water. In the top left plot, this tensor component shows no poles, whereas in the top right plot with a different orientation of water, a pole at 8.62 eV appears. A similar behavior can be observed for the  $\alpha_{yy}(\omega)$  component of benzene with the pole at 6.57 eV in the bottom

right plot. This clearly demonstrates that the pole positions of the polarizability tensor diagonal elements are not rotationally invariant. However, as Fig. 1 shows, the poles of the average dynamical polarizabilities are rotationally invariant as expected.

Figure 1 also shows that the  $\bar{\alpha}(\omega)$  poles define the RPA excitation energies (with nonvanishing intensities) calculated according to Eq. (32) or Eq. (38). Thus, these excitation energies are indeed determined by the poles of a ground state property, namely the average dynamical polarizability. Note that this does not hold for the corresponding TDA excitation energies (blue vertical lines in Fig. 1). As Fig. 1 shows they are often shifted to higher energies, albeit not homogeneously. By removing the indetermination from the average dynamical polarizability at the position of a given pole,  $\bar{\alpha}(\omega_I)$ , i.e., the residue of  $\bar{\alpha}(\omega)$  at  $\omega_I$ , the expression for the TDDFT oscillator strength,  $f_\lambda$ , is obtained,

$$f_\lambda(\omega_I) = \frac{2}{3} \left[ \sum_i^{\text{occ uno}} \sum_a^{\text{x,y,z}} \left( X_{ai}^{(\lambda)}(\omega_I) + Y_{ai}^{(\lambda)}(\omega_I) \right) \Gamma_{ai}^{(\lambda)} \right]^2. \quad (43)$$

In Eq. (43),  $\lambda$  corresponds to the axis in which the pole appeared of the dynamic polarizability elements. Note that the information of  $\lambda$  in  $X_{ai}^{(\lambda)}(\omega)$  and  $Y_{ai}^{(\lambda)}(\omega)$  is lost because Eq. (32) is independent of  $\Gamma_{ai}^{(\lambda)}$ , which carries the  $\lambda$  dependency. Thus, oscillator strengths are usually calculated using an analog to the sum-over-states expression,<sup>31</sup>

$$f_I = \frac{2}{3} \sum_\lambda^{\text{x,y,z}} \left[ \sum_i^{\text{occ uno}} \sum_a^{\text{x,y,z}} \left( X_{ai}^{(\lambda)}(\omega_I) + Y_{ai}^{(\lambda)}(\omega_I) \right) \Gamma_{ai}^{(\lambda)} \right]^2. \quad (44)$$

Equation (43) implies that excitations with large oscillator strength correspond to poles of the dynamic polarizability with large residues whereas excitations with small enough oscillator strengths might not have a visible pole. With the aim to demonstrate the relationship between the oscillator strengths and the residues of the poles, we performed RPA and TDA TDADFT calculation on norbornadiene employing the VWN<sup>33,34</sup>/DZVP<sup>37</sup>/GEN-A2<sup>#36</sup> level of theory. Figure 2 plots the RPA (red) and TDA (blue) oscillator

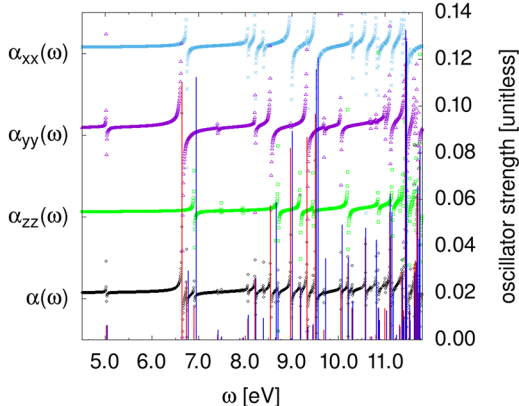


**FIG. 2.** Dynamic polarizability of norbornadiene molecule. Excitation energies calculated using RPA and TDA TDADFT are shown with red and blue vertical lines, respectively. The scale of the oscillator strength is shown on the right.

strengths as vertical lines according to the unitless scale shown at the right side of the figure.

As anticipated from Eq. (43), the poles with large residues correspond to excitations with larger oscillator strengths and poles with smaller residues, which are harder to observe, correspond to excitations with smaller oscillator strengths. Figure 2 also shows that the TDA oscillator strengths (blue vertical lines) differ from those of the RPA (red vertical lines) and cannot always be related to the pole positions and residues of the average dynamical polarizability. In fact, Rocca *et al.*<sup>38</sup> showed that the TDA does not fulfill the Thomas-Reiche-Kuhn sum rule,<sup>39</sup> which renders the oscillator strengths less reliable. We also note that the differences in the oscillator strengths do not necessarily correlate with the differences of the corresponding excitation energies for these two methods.

### III. IMPLEMENTATION DETAILS

The computational performance of TDADFT is mainly determined by the matrix vector multiplications in the Davidson diagonalizer. As already discussed by Carmona-Espíndola *et al.*,<sup>26</sup> the three-center ERIs have to be build twice in each matrix-vector multiplications. Thus, efficient ERI algorithms with low-order scalings are mandatory for computationally potent TDADFT implementations. To this end, we use in our new TDADFT implementation floating point (FLOP) operation optimized three-center ERI recurrence relations in combination with corresponding double asymptotic expansions. For clarity of discussion, we use in the following the TDA equation system, Eq. (41), and omit spin dependencies as well as the initial diagonal term of the  $A$  matrix. Thus, the closed-shell matrix vector multiplication is given by

$$X'_{ai} = \sum_j^{\text{occ uno}} \sum_b^{\text{x,y,z}} B_{ai,bj} X_{bj}. \quad (45)$$

Here,  $X_{bj}$  are the elements of the initial trial vector, and  $X'_{ai}$  are the elements of the resulting vector. Expanding the  $B$  matrix elements yields

$$\begin{aligned} X'_{ai} = & 2 \sum_{\mu,\nu} c_{\mu a} c_{\nu i} \sum_k \langle \mu\nu \parallel \bar{k} \rangle \sum_{\bar{l}} G_{\bar{k}\bar{l}}^{-1} \sum_{\sigma,\tau} \langle \bar{l} \parallel \sigma\tau \rangle \\ & \times \sum_j^{\text{occ uno}} \sum_b^{\text{x,y,z}} c_{\sigma b} c_{\tau j} X_{bj} + 2 \sum_{\mu,\nu} c_{\mu a} c_{\nu i} \sum_k \langle \mu\nu \parallel \bar{k} \rangle \sum_m G_{\bar{k}\bar{m}}^{-1} \\ & \times \sum_{\bar{n}} \langle \bar{m} | f_{xc}[\tilde{p}] | \bar{n} \rangle \sum_{\bar{l}} G_{\bar{n}\bar{l}}^{-1} \sum_{\sigma,\tau} \langle \bar{l} \parallel \sigma\tau \rangle \sum_j^{\text{occ uno}} \sum_b^{\text{x,y,z}} c_{\sigma b} c_{\tau j} X_{bj}. \end{aligned} \quad (46)$$

In Eq. (46), we have separated the Coulomb and exchange-correlation part of the matrix vector multiplication and have positioned the summations according to their on-the-fly execution.

Starting from right to left, we first transform the excitation vector elements  $X_{bj}$  into AO representation,

$$X_{\sigma\tau} = \sum_j^{\text{occ uno}} \sum_b^{\text{x,y,z}} c_{\sigma b} c_{\tau j} X_{bj}. \quad (47)$$

This step possesses a formal cubic scaling. Basic linear algebra subprogram (BLAS) subroutines are used to obtain the maximum

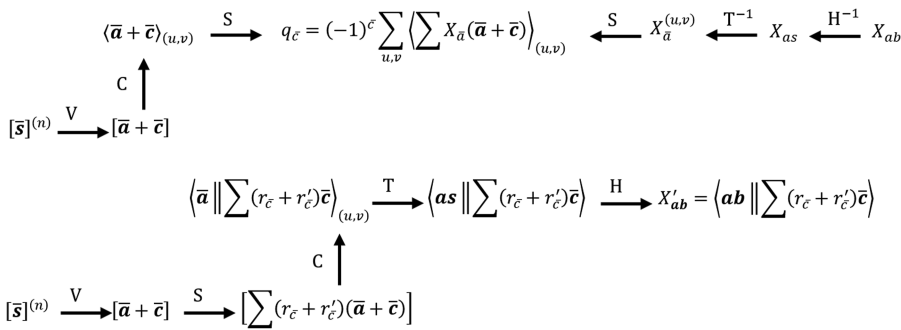


**FIG. 3.** Pathway diagrams for the near field three-center electron repulsion integral sums in Eq. (48), top, and Eq. (53), bottom. Further details are given in Ref. 22.

FLOP rate of the processors in this step. Therefore, it has, in practice, almost no effect on the computational scaling for the here discussed system sizes. In the following step, the  $X_{\sigma\tau}$  elements are multiplied with the three-center ERIs,

$$q_{\bar{l}} = \sum_{\sigma,\tau} \left\langle \bar{l} \parallel \sigma\tau \right\rangle X_{\sigma\tau}, \quad (48)$$

In our new implementation, the ERIs can be either stored in RAM (Conventional) or calculated on-the-fly according to the pathway diagram in the top of Fig. 3. Furthermore, the near field ERI calculation can be combined with the double asymptotic expansion for far field ERIs yielding the so-called Mixed or Multipole approaches, respectively. The pathway diagram for the double asymptotic ERI expansion in the summation of Eq. (48) is given in the top of Fig. 4.

To proceed, the resulting auxiliary function vector  $\mathbf{q}$  is multiplied with the inverse Coulomb matrix  $\mathbf{G}^{-1}$ ,

$$r_{\bar{k}} = \sum_{\bar{l}} G_{\bar{k}\bar{l}}^{-1} q_{\bar{l}}. \quad (49)$$

For large systems with more than 50 000 auxiliary functions, the explicit construction of  $\mathbf{G}^{-1}$  becomes a computational bottleneck. Therefore, we also implemented the MINRES solver for the equation system,

$$\sum_{\bar{l}} G_{\bar{k}\bar{l}} r_{\bar{l}} = q_{\bar{k}}. \quad (50)$$

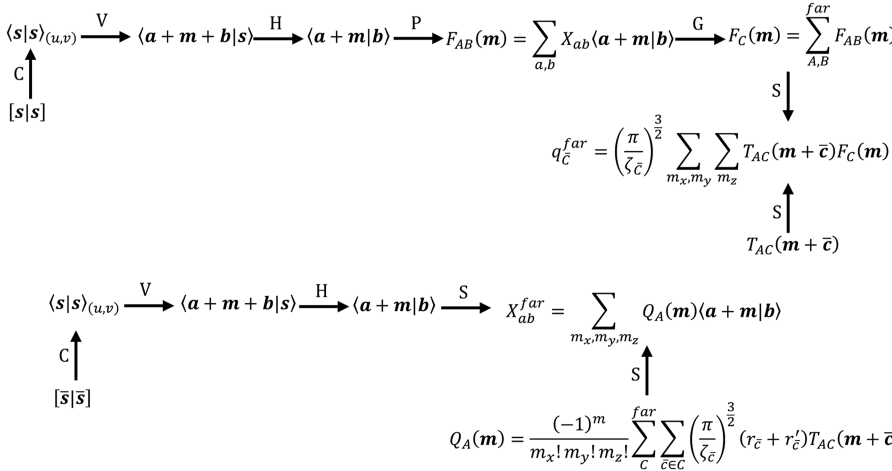


**FIG. 4.** Pathway diagrams for the far field three-center electron repulsion integral sums in Eq. (48), top, and Eq. (53), bottom, using the double asymptotic ERI expansion. Further details are given in Ref. 23.

For this second ERI calculation, all four ERI options, i.e., Conventional, Direct, Mixed, and Multipole are available, too.

The pathway diagram for near field ERI calculation of the sum in Eq. (53) is given in the bottom of Fig. 3, whereas the corresponding pathway diagram for the double asymptotic expanded far field ERIs is given in the bottom of Fig. 4.

The matrix vector multiplication in the Davidson cycle is concluded by transforming  $X'_{\mu\nu}$  into MO representation,

$$X'_{ai} = 2 \sum_{\mu,\nu} c_{\mu a} c_{\nu i} X'_{\mu\nu} \quad (54)$$

As the first step of the matrix vector multiplication, Eq. (47), this step possesses a formal cubic scaling. However, it has, in practice, almost no effect on the computational scaling because of the use of BLAS subroutines. The factor 2 in Eq. (54) accounts for the double occupation of spatial MOs in closed-shell.

As can be expected from this discussion, the computational performance of the matrix vector multiplication and, thus of the Davidson diagonalizer, is mainly determined by the algorithms used for the two ERI summations, Eqs. (48) and (53).

#### IV. COMPUTATIONAL DETAILS

All auxiliary density functional theory (ADFT) calculations were performed using a local modified version of the deMon2k code, version 6.2.2.<sup>40</sup> As outlined in Sec. III, the calculation of four-center electron repulsion integrals (ERIs) and four-center kernel integrals is avoided in TDADFT. To analyze the effects of this computational simplification, we compare deMon2k TDADFT results with corresponding four-center ERI and kernel calculations obtained with NWChem, version 6.8.<sup>41</sup> In these calculations, the PBE functional in combination with the aug-cc-pVTZ<sup>35</sup> basis set was used. In all deMon2k TDADFT calculations, the automatically generated GEN-A2\*<sup>36</sup> auxiliary function set was employed. For the TDADFT calculations, the Davidson pseudo-diagonalization<sup>42</sup> as outlined by Carmona-Espíndola and Köster<sup>21</sup> was used. The on-the-fly matrix vector multiplications are performed according to the previously given implementation details. For the validation of TDADFT, the valence excitations of the test sets from Tozer,<sup>43</sup> Thiel,<sup>44</sup> and Jacquemin<sup>45,46</sup> were used. Thus, our test set consists of 57 molecules with together 130 singlet and 93 triplet valence excitations. The reference data are either from experiment or high-level wave function calculations. For the TDADFT validation, we first optimized the molecular structures at the PBE<sup>47</sup>/aug-cc-pVTZ<sup>35</sup>/GEN-A2\*<sup>36</sup> level of theory. For the subsequent excited state calculations the following five exchange-correlation functionals were used: Dirac exchange<sup>33</sup> with VWN correlation,<sup>34</sup> referred to as VWN hereafter; PBE<sup>47</sup>; B88 exchange<sup>48</sup> with P86 correlation,<sup>34,49</sup> referred to as BP86 hereafter; CAP;<sup>50</sup> and NCAP.<sup>51</sup> The Kohn-Sham wave function was expanded with the DZVP<sup>37</sup> and DZVP-GGA<sup>36</sup> basis sets for LDA and GGA calculations, respectively, as well as with the aug-cc-pVTZ<sup>35</sup> basis set.

For the performance analysis of the newly implemented three-center ERI options, four sets of molecules were used: alkane chains, fullerene molecules,<sup>52</sup> DNA fragments,<sup>53</sup> and zeolites. All TDADFT excitations and timings refer to deMon2k calculations whereas TDDFT results refer to NWChem calculations if not otherwise

stated. The performance analysis calculations were performed on nodes with 24 Intel(R) Xeon(R) E5-2650 v4 @ 2.20 GHz cores with 5 GB of RAM memory per core. All alkane calculations were performed on one node, i.e., on 24 cores. For the fullerene and DNA calculations, we used two nodes with together 48 cores. Finally, for the zeolite calculations, we used four nodes that account for 96 cores. The level of theory was PBE/DZVP-GGA/GEN-A2 for all performance analysis calculations. The auxiliary density exchange-correlation kernel was read from hard disk, and the explicit inversion of the Coulomb matrix, Eqs. (49) and (52), was used in all calculations unless otherwise noted. For the timing comparison between TDDFT and TDADFT a node with 16 Intel(R) Xeon(R) E5-2650 v2 cores with 4 GB of RAM per core was employed. The level of theory for these calculations was PBE/6-311G\* using the auxiliary function set GEN-A2\* for the TDADFT calculations.

The illustrative BOMD simulations were carried out on a few simple molecules for which experimental spectra are available at the PBE<sup>47</sup>/DZVP-GGA<sup>36</sup>/GEN-A2\*<sup>36</sup> level of theory. The simulations were performed in the canonical (NVT) ensemble at various temperatures. The temperature was controlled with a three chain Nosé-Hoover thermostat.<sup>54–56</sup> The step size was set to 1 fs. In the benzene, naphthalene and anthracene BOMD simulations 100 000 propagation steps were recorded. In a second run, TDADFT calculations were performed in 100 step intervals along these recorded trajectories. In each of these TDADFT calculations, 600 excitations were evaluated for benzene and naphthalene, whereas 700 were evaluated for anthracene. The absorption spectrum was constructed following closely the histogram-spectrum procedure from Moseler *et al.*<sup>57</sup> To this end, the energy window of the spectra is divided in intervals of fixed width,  $\Delta\omega = 0.025$  eV. For each interval,  $\Delta\omega_i$ , the oscillator strengths of all excitations within this energy interval are added. This process is repeated for each time step,  $t_s$ , for which TDADFT calculations are performed. Thus, the absorption spectrum is constructed as

$$\sigma(\Delta\omega_i) = \frac{1}{n} \sum_{t_s}^n \sum_I^{w_I^{t_s} \in \Delta\omega_i} f_I(t_s). \quad (55)$$

In Eq. (55),  $n$  denotes the number of TDADFT calculations along the BOMD trajectory. In a separated calculation, the spectra of all three aromatics were calculated at the PBE/DZVP-GGA/GEN-A2\* level of theory using the ground state optimized structures at the same level of theory. These spectra are plotted using vertical red lines with a height relative to the oscillator strength.

#### V. RESULTS AND DISCUSSION

##### A. Validation of TDADFT

We start our validation with a comparison of TDADFT and TDDFT employing the PBE/aug-cc-pVTZ level of theory. To this end, we calculated with both approaches the first 30 singlet and triplet excitations of water, ethene, *E*-butadiene, adenine, formamide, and thioacetone. Figure 5 plots the TDADFT excitation energies from these systems against those calculated with TDDFT. The calculated excitation energies for this plot are listed in Table S1 of the *supplementary material*. As this figure shows that an almost perfect linear regression is found with a correlation coefficient of 0.9991. The corresponding mean absolute error (MAE) and mean

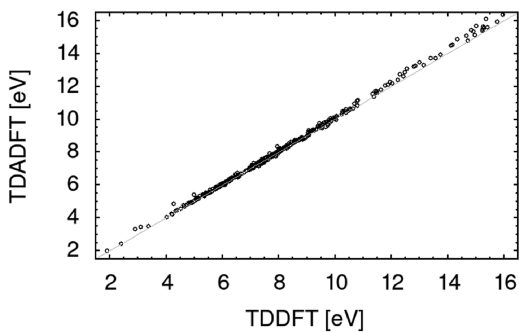


**FIG. 5.** Linear correlation between TDADFT and TDDFT excitation energies using the PBE functional and the aug-cc-pVTZ basis set. The sample consists of 180 singlet and 180 triplet excitations. See text for details.

signed error (MSE) of 0.12 and +0.11 eV, respectively, indicate that TDADFT excitation energies are slightly shifted with respect to their TDDFT references by around +0.1 eV. Thus, TDADFT reproduces TDDFT results to good accuracy, albeit with a greatly reduced computational demand.

For a broader validation of valence excitations, we studied 223 excitations, namely 130 singlet and 93 triplet excitations of 57 molecules. The errors were calculated with respect to high-level wave function reference data. Table S2 of the [supplementary material](#) lists the calculated TDADFT excitation energies together with corresponding high-level theoretical and experimental reference data from the literature. From these data, the MSE and MAE were calculated for TDADFT RPA and TDA excitations and are plotted at the top and bottom of Fig. 6, respectively. In this figure, we use dark colored error bars for singlet and light colored error bars for triplet excitations. The analysis was performed with two different basis sets, DZVP<sup>36,37</sup> (left) and aug-cc-pVTZ<sup>35</sup> (right). As Fig. 6 shows, the

MAE of TDA valence excitations are always smaller than the corresponding RPA MAE. The reason is the systematic underestimation of the excitation energies by RPA TDADFT as shown by the MSE in Fig. 6. Thus, the already discussed shift of TDA TDADFT excitations to higher energies<sup>16,17,58</sup> (see Figs. 1 and 2) slightly improves the MAE of TDA with respect to RPA. This effect is for the larger aug-cc-pVTZ basis set more pronounced than for the DFT optimized DZVP basis sets. We also note that the DFT optimized basis sets perform consistently better than the aug-cc-pVTZ one. On the other hand, the asymptotically corrected CAP and NCAP functionals show similar performances as other GGAs. The detailed statistical analyses for the valence excitations can be found in Tables S3–S6 of the [supplementary material](#).

To put these TDADFT results in perspective, we compare them in Tables I and II with TDDFT results from the literature. Table I lists MSE for singlet valence excitations. As this table shows, the TDADFT DZVP-GGA results are in good agreement with corresponding literature data. Note that the extension of the basis set to aug-cc-pVTZ increases the MSE by roughly 0.1 eV. These results for the TDADFT singlet valence excitations underline the good agreement between TDADFT and TDDFT once again. Table II lists MSE for corresponding triplet excitations. Again, the comparison with literature data show generally good agreements. An exception is PBE, where TDADFT improves by about 0.2 eV over corresponding TDDFT literature data. In addition, note that for triplet excitations the extension of the basis set has much smaller effects on the MSE as for singlet excitations.

## B. Performance analysis

We begin the performance analysis by the comparison of different methodologies for the evaluation of three-center ERIs in *n*-alkane chains. The ERI calculations are in-core storage (Conventional), on-the-fly evaluation (Direct), on-the-fly near field evaluation with the double asymptotic expansion for far field ERIs (Multipole), and in-core storage of near field ERIs with double asymptotic expansion for far field ERIs (Mixed). To simplify the

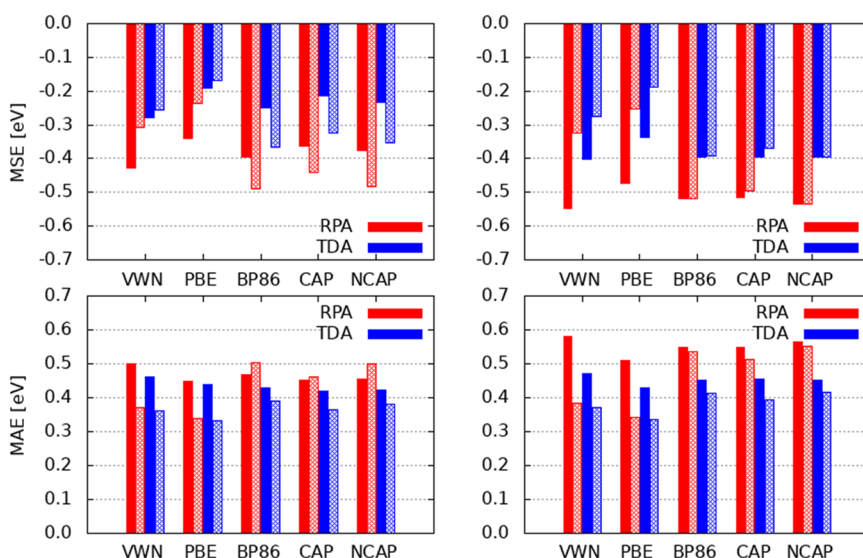


**FIG. 6.** MSE and MAE of 130 singlet (dark) and 93 triplet (light) valence excitations using DZVP (left column) and aug-cc-pVTZ (right column) basis sets.

**TABLE I.** Comparison of TDADFT singlet valence excitation MSEs with corresponding TDDFT literature results. The TDADFT MSEs refer to DZVP and aug-cc-pVTZ (values in parentheses) basis sets. The data used to calculate the MSEs are given in the references below the table.

	RPA		TDA	
	TDADFT	TDDFT	TDADFT	TDDFT
VWN	-0.43 (-0.55)	-0.49 <sup>a</sup>	-0.28 (-0.40)	...
PBE	-0.34 (-0.47)	-0.46 <sup>a</sup> , -0.48 <sup>b</sup>	-0.19 (-0.34)	-0.32 <sup>b</sup>
BP86	-0.39 (-0.52)	-0.44 <sup>c</sup>	-0.25 (-0.40)	...

<sup>a</sup>TZVP from Maier *et al.*<sup>17</sup>

<sup>b</sup>aug-cc-pVTZ from Peach and Tozer.<sup>59</sup>

<sup>c</sup>TZVP from Silva-Junior *et al.*<sup>60</sup>

**TABLE II.** Comparison of TDADFT triplet valence excitation MSEs with corresponding TDDFT literature results. The TDADFT MSEs refer to DZVP-GGA and aug-cc-pVTZ (values in parentheses) basis sets. The data used to calculate the MSEs are given in the references below the table.

	RPA		TDA	
	TDADFT	TDDFT	TDADFT	TDDFT
VWN	-0.31 (-0.32)	-0.34 <sup>a</sup>	-0.26 (-0.27)	...
PBE	-0.23 (-0.25)	-0.50 <sup>a</sup> , -0.43 <sup>b</sup>	-0.17 (-0.19)	-0.34 <sup>b</sup>
BP86	-0.4 <sup>b</sup> (-0.52)	-0.53 <sup>c</sup>	-0.37 (-0.39)	...

<sup>a</sup>TZVP from Maier *et al.*<sup>17</sup>

<sup>b</sup>aug-cc-pVTZ from Peach and Tozer.<sup>59</sup>

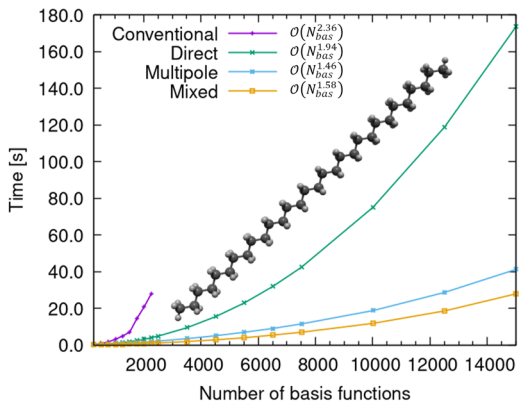
<sup>c</sup>TZVP from Silva-Junior *et al.*<sup>60</sup>

discussion, only the averaged time for a single on-the-fly TDADFT matrix-vector multiplication is shown in Fig. 7.

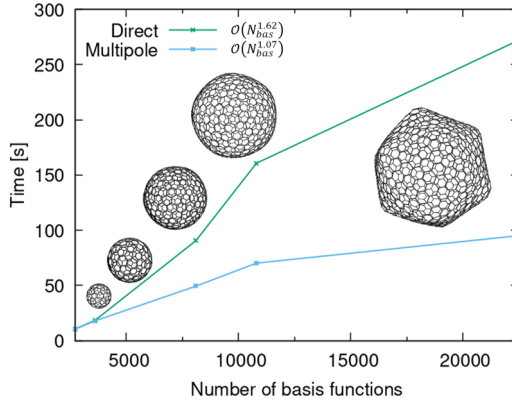
In the Conventional approach, the three-center ERIs are calculated once and stored in RAM. Because the ERI calculation is already performed in the SCF, it is not accounted here. However, we only allow Conventional calculations with in-core storage. This significantly limits the applications range of this ERI approach as

Fig. 7 shows. The largest alkane possible to calculate with the Conventional option on the here used architecture is C<sub>100</sub>H<sub>202</sub>. Despite the fact that the ERIs have not to be recalculated in the Conventional approach, it shows the largest scaling of 2.36 for the TDADFT matrix-vector multiplication. This is rooted in the evaluation of the sums in Eqs. (48) and (53), which are performed explicitly over all atomic orbitals and auxiliary functions in the Conventional approach. Although in the Direct approach ERIs are recalculated in each matrix-vector multiplication the scaling is reduced to 1.94 as Fig. 7 shows. The reason for the reduced scaling of the Direct approach with respect to the Conventional one is the inverse horizontal and transformation recurrence relations (Fig. 3, top) for the calculation of the sum in Eq. (48) and the early summations of the auxiliary functions (Fig. 3, bottom) for the sum in Eq. (53). Thus, a large part of these integral summations possesses in the Direct approach a formal quadratic rather than cubic scaling. A further reduction of the scaling of the matrix-vector multiplication is observed if the double asymptotic expansion for far field three-center ERIs is activated, i.e., in the Multipole and Mixed approaches. Here, far field three-center ERIs are calculated with the linear scaling methodology shown in Fig. 4. Due to the increased proportion of far field ERIs with system size, the scaling is lowered to 1.46 in the Multipole and 1.58 in the Mixed approach, respectively. Because of the memory demand of the Conventional and Mixed approaches, we will not study them for larger systems. Figure 8 shows the computational timings for the matrix-vector multiplications in fullerenes. Most notable is the scaling reduction from C<sub>720</sub>. It indicates the transition from a 3D to a 2D system for the molecular integral calculation. The observed scalings for the matrix-vector multiplications are 1.62 and 1.07 for the Direct and Multipole approach, respectively.

The timings for the TDADFT matrix-vector multiplications in DNA fragments are shown in Fig. 9. The Direct and Multipole approaches show larger scalings than for the previous two systems despite the fact that the proportion of near and far field ERIs in the DNA fragments is similar to that in the fullerenes. We attribute this to the geometrical extension of the DNA fragments, which grow three-dimensional.



**FIG. 7.** Computational time for a TDADFT matrix-vector multiplication on 24 cores of alkane chains with 10–600 carbon atoms. The observed scaling,  $\mathcal{O}(N_{\text{bas}}^{\chi})$ , is shown for each three-center ERI option, too.



**FIG. 8.** Computational time for a TDADFT matrix-vector multiplication on 48 cores for fullerenes with 180, 240, 540, 720, and 960 carbon atoms. The observed scaling  $\mathcal{O}(N_{\text{bas}}^{\chi})$  is shown for the Direct and Multipole ERI option.

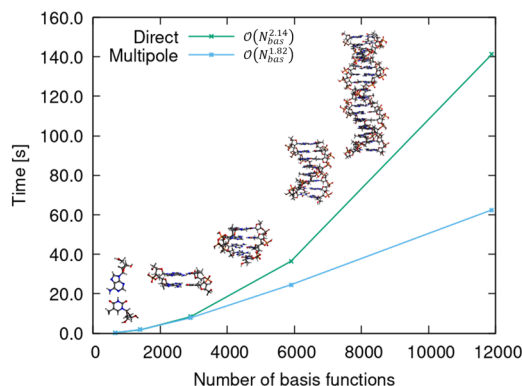


**FIG. 9.** Computational time for a TDADFT matrix-vector multiplication on 48 cores of DNA fragments with 1, 2, 4, and 16 base pairs. The observed scaling  $\mathcal{O}(N_{\text{bas}}^x)$  is shown for the Direct and Multipole ERI option.

Figure 10 displays the computational timings of TDADFT matrix-vector multiplications for hydrogen saturated MFI zeolite cutouts. These structures grow three-dimensional and are dense for the ERI calculations. Therefore, higher scaling as for the previous systems is expected. The observed scalings of 2.22 and 1.78 for the Direct and Multipole approach, respectively, are rather satisfying. This demonstrates that excited state calculations on systems with more than 1000 atoms are feasible in very reasonable times with TDADFT.

The performance of the MINRES implementation in TDADFT was evaluated using the MFI zeolite cutouts in combination with the auxiliary function set GEN-A2\*. The use of the MINRES method avoids the diagonalization of the two-center ERI matrix,  $\mathbf{G}$ , needed for the truncated eigenvalue decomposition (TED). The trade off when using MINRES is the number of MINRES iterations that can be large. Therefore, we show in Table I the time contribution of MINRES to the matrix vector multiplication. This table also shows the size of the Coulomb matrix (column 3), the time for the TED diagonalization of  $\mathbf{G}$  (column 4), and the RAM demand of TED and

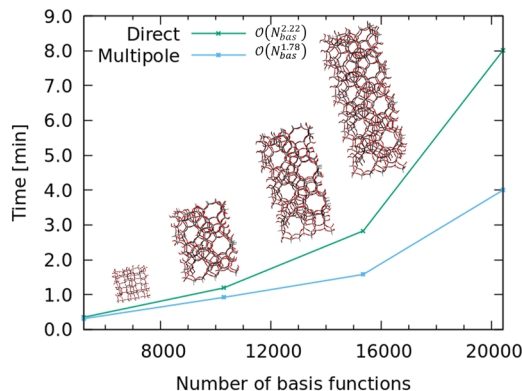


**FIG. 10.** Computational time for a TDADFT matrix-vector multiplication on 96 cores for zeolite cutouts with 376, 720, 1064, and 1408 atoms. The observed scaling  $\mathcal{O}(N_{\text{bas}}^x)$  is shown for the Direct and Multipole ERI option.

**TABLE III.** Number of atoms,  $N_{\text{atom}}$ , number of auxiliary functions,  $N_{\text{aux}}$ , size in GB of the two-center ERI matrix,  $\mathbf{G}$ , time in hours for the TED diagonalization of  $\mathbf{G}$ , (TED), time in seconds for MINRES, RAM per core needed for solving the explicit diagonalization (TED), and for MINRES for MFI zeolite cutouts using 96 cores.

$N_{\text{atom}}$	$N_{\text{aux}}$	Size (GB)	Time		Memory/core (MB)	
			TED (h)	MINRES (s)	TED	MINRES
376	33 608	8.4	1.56	0.75	90.07	6.07
720	66 512	33.0	11.68	1.00	352.15	12.6
1064	99 416	73.6	51.87	1.23	786.32	18.24

MINRES. Since diagonalization of  $\mathbf{G}$  is performed before the SCF the use of MINRES reduces the total calculation time by roughly the time given in column 4 of Table III.

Note that for smaller systems, where the diagonalization of the  $\mathbf{G}$  matrix takes only a few seconds, the explicit diagonalization of  $\mathbf{G}$  is the most efficient method. As a rule of thumb, MINRES is advised when more than 50 000 auxiliary functions are used.

To put the here reported timings of TDADFT into context, the computational time for the TDADFT matrix-vector multiplication is compared in Fig. 11 with corresponding TDDFT timings for a series of alkane chains. As this figure shows, TDADFT is always faster than its four-center TDDFT counterpart and shows a substantially reduced scaling of 1.32 against 2.42. Furthermore, the TDDFT system size is limited to around 2000 basis functions with the here used computational resources whereas TDADFT reaches the series end of 300 carbon atoms without problems.

We finish our performance analysis of TDADFT by evaluating the efficiency of its MPI parallelization in deMon2k. To this end, we run TDADFT calculations of the MFI zeolite cutout with 720 atoms using 12, 24, 48, 96, and 144 Intel(R) Xeon(R) E5-2650 v4 @ 2.20 GHz processors. Figure 12 compares the deMon2k parallelization with the ideal one. As this figure shows, an almost ideal scaling with respect to the number of processors is found until 48 cores. For

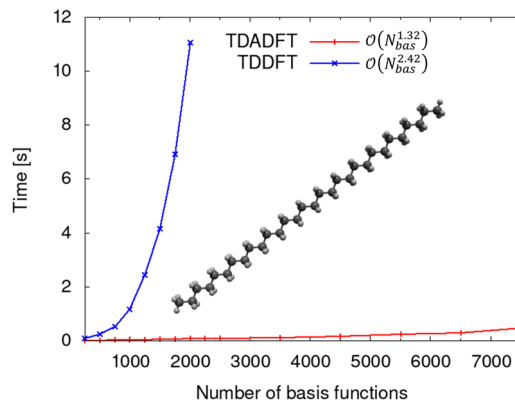


**FIG. 11.** Comparison of the computational timings for three-center TDADFT (deMon2k) and four-center TDDFT (NWChem) matrix-vector multiplications on 16 cores for a series of n-alkane chains with up to 300 carbon atoms. Calculations are performed at the PBE/6-311G\* level of theory using the GEN-A2\* auxiliary function set in TDADFT.

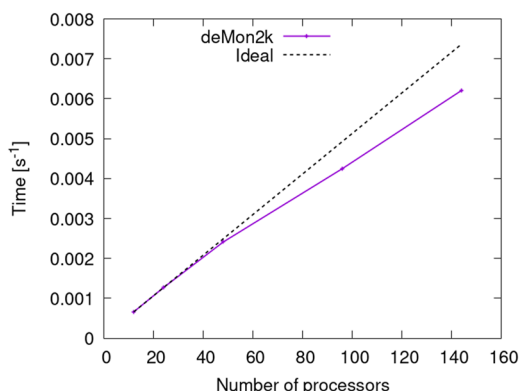


**FIG. 12.** Reciprocal CPU time for a matrix-vector multiplication of the TDADFT matrix of the 720 atoms MFI zeolite cutout using 12, 24, 48, 96, and 144 processors.

larger numbers of cores, the parallelization slightly deteriorates but still shows very acceptable scaling behavior.

### C. Born-Oppenheimer molecular dynamics

The efficiency of TDADFT permits to calculate a large number of spectra with relatively moderate computational cost. This is particularly useful for the incorporation of temperature effects through the calculation of spectra along BOMD trajectories. As illustrative examples, we present in the following temperature effects on the spectra of benzene, naphthalene, and anthracene. To this end, we calculated the spectra of these molecules at different temperatures from corresponding BOMD runs. To evaluate the effect of the temperature, we compare these spectra with the one at 0 K calculated at the ground state optimized geometry. The accuracy of the calculated spectra is then evaluated by comparison with the experimentally recorded spectrum for each of the three molecules.<sup>61–63</sup> We start with benzene. Figure 13 compares the calculated and experimental spectra of benzene. The excitation spectrum calculated at 0 K

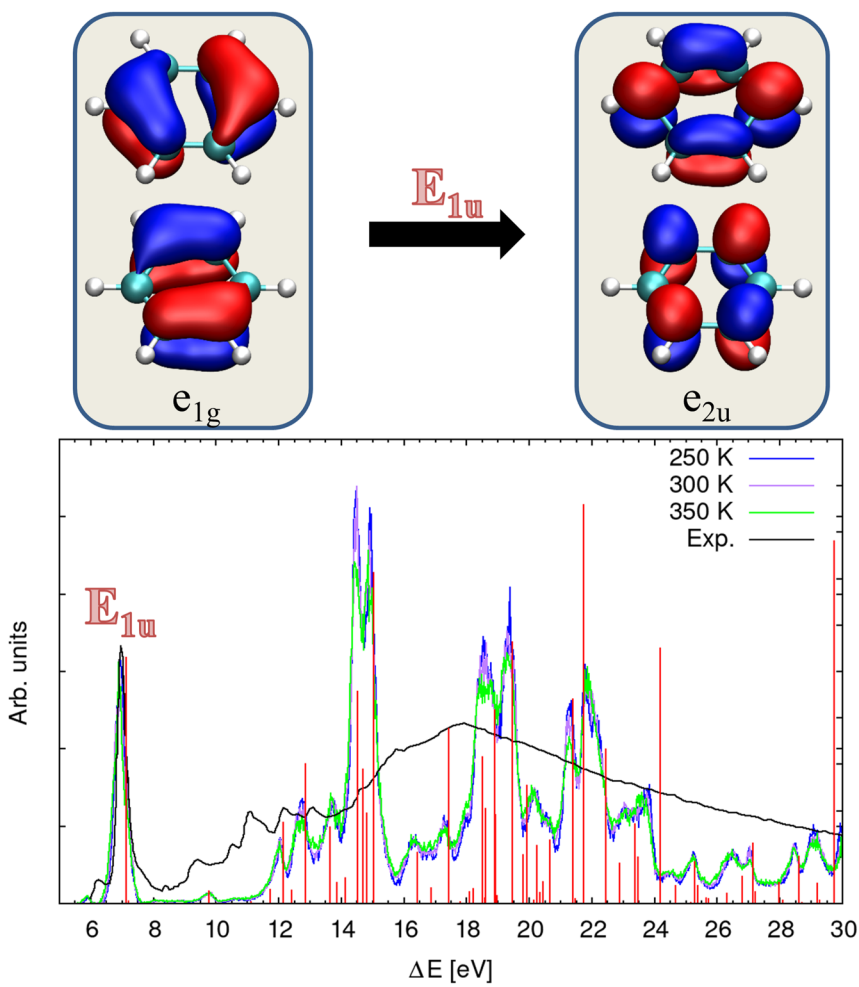


**FIG. 13.** The top insert shows the MOs involved in the  $E_{1u}$  excitation of the bottom insert. The bottom insert shows the experimental absorption spectra of benzene<sup>61</sup> (black) and calculated spectra at different temperatures (blue to green). The 0 K spectrum is plotted with vertical red lines.

with the optimized ground state geometry is shown by vertical red lines, too. The symmetry assignment for the first visible excitation of the 0 K spectrum is also shown. For this excitation, the relevant MOs are plotted at the top of Fig. 13. As the benzene spectra at the bottom of Fig. 13 shows, temperature has no effect on the peak positions. However, it changes relative intensities. Comparison with the experiment reveals an excellent agreement in position and shape for the first large peak at 7 eV. This excitation corresponds to a  $\pi \rightarrow \pi^*$  transition between the degenerated HOMOs with  $e_{1g}$  symmetry and the degenerated LUMOs with  $e_{2u}$  symmetry. For the higher energetic excitations, the calculated spectra show a qualitatively satisfactory match to the experimental spectrum.<sup>61</sup>

The calculated and experimental spectra of naphthalene<sup>62</sup> are shown in the bottom insert of Fig. 14. The excitation spectrum calculated at 0 K with the optimized ground state structure is shown in red. Symmetry assignments for the two excitations with strongest intensities are shown in this figure, too. For these excitations, the relevant MOs are plotted in the top insert of Fig. 14.

Different from benzene the spectrum of naphthalene shows temperature dependency. The dominant  $B_{3u}$  and  $B_{1u}$  excitations shift to lower energies with increasing temperature. Unlike benzene, the naphthalene molecule can bend around the axis formed by the two bridge carbon atoms. This movement is sensitive to temperature and has a notable effect on the spectra. Given the observed

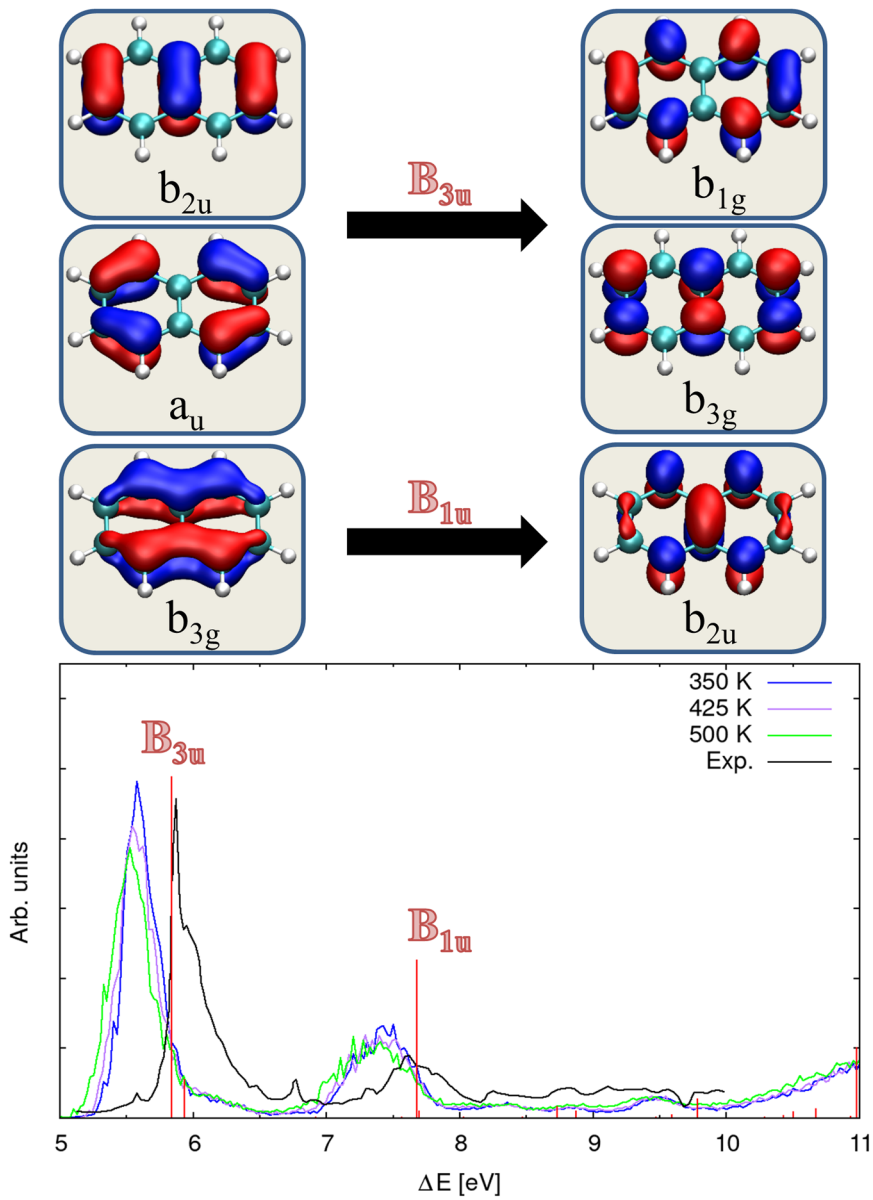


**FIG. 14.** The top insert shows the MOs involved in the  $B_{3u}$  and  $B_{1u}$  excitations of the bottom insert. The bottom insert shows the experimental absorption spectra of naphthalene<sup>62</sup> and calculated spectra at different temperatures. The 0 K spectrum is plotted with vertical red lines.

temperature dependency of the spectrum, it can be concluded that the experimental spectrum was recorded at low temperatures. Unfortunately, there is no information on the temperature of the experiment. In addition to the temperature dependent energy shift of the spectra, the shape of the largest peaks in the experimental spectrum at 6 and 7.7 eV are well represented by all BOMD simulated spectra. The first excitation corresponds to a  $B_{3u}$  transition. The dominant MO transitions for this excitation are  $b_{2u} \rightarrow b_{1g}$  and  $a_u \rightarrow b_{3g}$ . They are depicted in the top insert of Fig. 14. The second dominant excitation in the experimental spectrum corresponds to a  $B_{1u}$  transition. This excitation is dominated by  $b_{3g} \rightarrow b_{2u}$  MO transitions as shown by the lower part

of the top insert of Fig. 14. All relevant MO transitions account for  $\pi \rightarrow \pi^*$  excitations. As Fig. 14 shows, the inclusion of temperature also modulates the intensities to a qualitative good fit with the experiment.

The calculated and experimental spectra of anthracene<sup>63</sup> are shown in the bottom insert of Fig. 15. Again the 0 K excitation spectrum calculated at the optimized ground state structure is shown by red vertical lines. The symmetry assignment of the two dominant excitations reveals the same structure as for naphthalene, namely a  $B_{3u}$  and  $B_{1u}$  transition. For these excitations, the dominant MO transitions are plotted in the top insert of Fig. 15. The  $B_{3u}$  excitation is dominated by  $b_{1g} \rightarrow b_{2u}$  and  $b_{3g} \rightarrow a_u$  MO transitions, whereas the

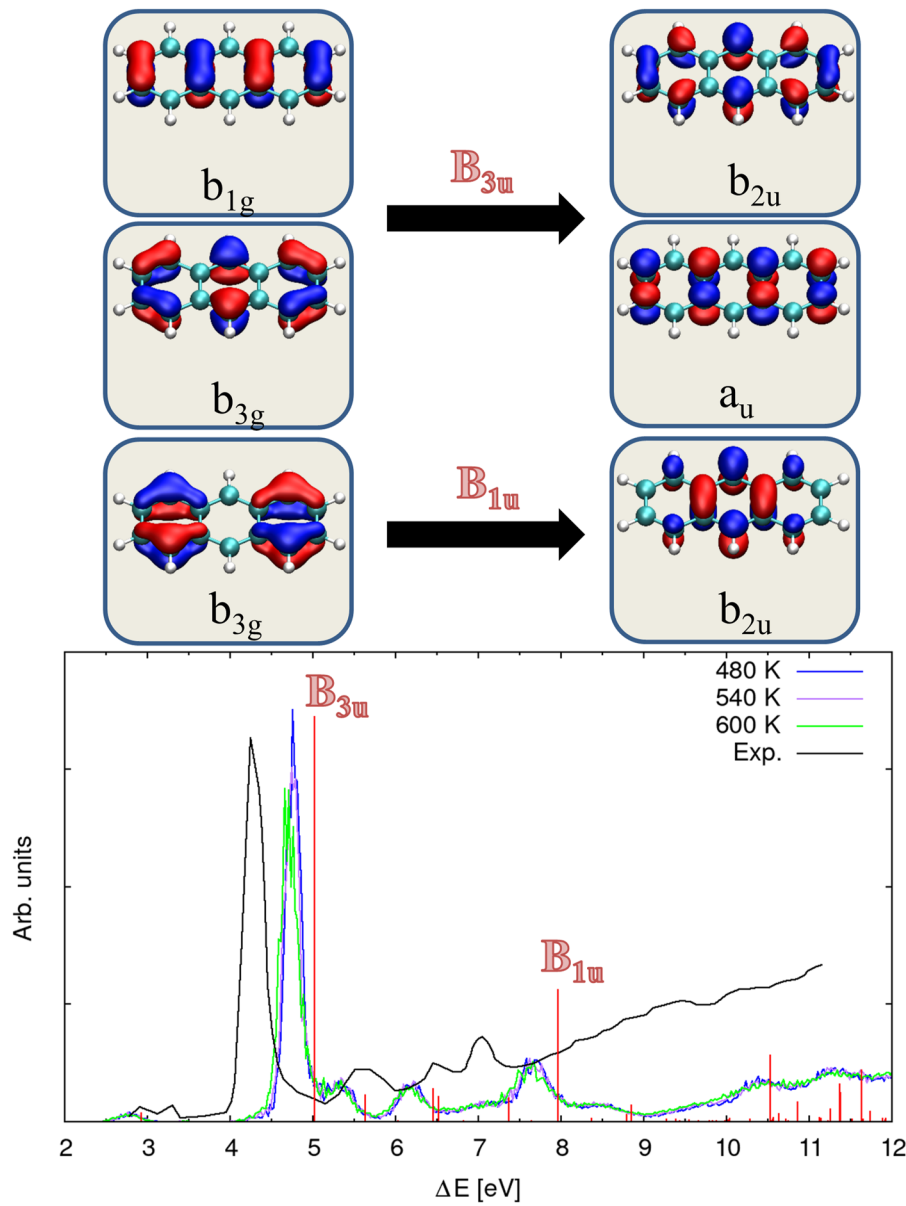


**FIG. 15.** The top insert shows the MOs involved in the  $B_{3u}$  and  $B_{1u}$  excitations of the bottom insert. The bottom insert shows the experimental absorption spectra of anthracene<sup>63</sup> and calculated spectra at different temperatures. The 0 K spectrum is plotted with vertical red lines.

$B_{1u}$  excitation is dominated by a  $b_{3g} \rightarrow b_{2u}$  MO transition. Again, these are  $\pi \rightarrow \pi^*$  excitations.

The temperature dependency of the anthracene spectrum (Fig. 15 bottom) is qualitatively the same as for naphthalene (Fig. 14 bottom), i.e., the emissions are shifted to lower energy with increasing temperature. Therefore, the same conclusions can be made, namely that the bending along the rings is responsible for the temperature dependency. In this case, the experiment was performed at high temperatures using an oven to evaporate the anthracene, which correlates correctly with the temperature trend observed in the energy shift of the calculated spectra. In addition to the energy shift, the shape of the first large peak at around 4.3 eV in the experimental spectrum is overall well described when temperature effects are included.

## VI. CONCLUSIONS

The RPA TDADFT working equations are derived from the ADPT formulation of dynamical polarizabilities. The rotational invariances of the dynamical polarizability pole structures and, thus, of the RPA excitation energies are demonstrated. The comparison of three-center TDADFT with four-center TDDFT excitation energies shows an almost perfect linear regression. A closer inspection reveals a small shift of +0.1 eV in the TDADFT excitation energies that results in an overall slightly better agreement with the experiment. The extension of the here outlined TDADFT implementation to hybrid functionals is currently under development in our laboratory. Our performance analysis shows that the computational scaling of TDADFT is subquadratic for all studied systems and that TDADFT calculations for system sizes of up to 20 000 basis functions are possible on processors with 5 GB/core RAM in very reasonable times using moderate parallel architectures.

The computational efficiency of the three-center TDADFT methodology permits large excitation energy range calculations along BOMD trajectories. The resulting absorption spectra include temperature and non-harmonic vibrational effects.<sup>64,65</sup> As illustrative examples, we present BOMD spectra simulations for benzene, naphthalene, and anthracene. An overall good qualitative agreement with experiment was observed for the three molecules when including temperature effects into the calculated spectra. Although benzene showed almost no shift of the emission bands with temperature, a notable shift to lower energies was found for naphthalene and anthracene.

## SUPPLEMENTARY MATERIAL

Tables of calculated excitation energies and statistical analyses are given in the [supplementary material](#).

## ACKNOWLEDGMENTS

This work was financially supported by the CONACyT project Grant No. A1-S-11929. Luis I. Hernández-Segura gratefully acknowledges a CONACyT Ph.D. fellowship (Grant No. 455854). The authors were grateful for the computing time granted by LANCAD and CONACYT in the supercomputer hybrid cluster “Xiuhcoatl” at General Coordination of Information and Communication Technologies (CGSTIC) of CINVESTAV.URL: <http://clusterhibrido.cinvestav.mx/>.

## AUTHOR DECLARATIONS

### Conflict of Interest

The authors have no conflicts to disclose.

### Author Contributions

**Luis I. Hernández-Segura:** Conceptualization (equal); Data curation (equal); Formal analysis (equal); Investigation (equal); Methodology (equal); Software (equal); Validation (equal); Writing – original draft (equal); Writing – review & editing (equal). **Andreas M. Köster:** Conceptualization (equal); Formal analysis (equal); Funding acquisition (equal); Investigation (equal); Methodology (equal); Project administration (equal); Software (equal); Supervision (equal); Writing – original draft (equal); Writing – review & editing (equal).

## DATA AVAILABILITY

The data that support the findings of this study are available within the article and its [supplementary material](#).

## REFERENCES

- <sup>1</sup>M. Petersilka, U. J. Gossmann, and E. K. U. Gross, *Phys. Rev. Lett.* **76**, 1212 (1996).
- <sup>2</sup>D. Escudero, A. D. Laurent, and D. Jacquemin, in *Handbook of Computational Chemistry*, edited by J. Leszczynski, A. Kaczmarek-Kedziera, T. Puzyń, M. G. Papadopoulos, H. Reis, and M. K. Shukla (Springer International Publishing, Cham, 2017), pp. 927–961.
- <sup>3</sup>F. C. Grozema, R. Teleshca, H. T. Jonkman, L. D. A. Siebbeles, and J. G. Snijders, *J. Chem. Phys.* **115**, 10014 (2001).
- <sup>4</sup>F. Furche and R. Ahlrichs, *J. Chem. Phys.* **117**, 7433 (2002).
- <sup>5</sup>B. G. Levine, C. Ko, J. Quenneville, and T. J. Martínez, *Mol. Phys.* **104**, 1039 (2006).
- <sup>6</sup>Y. Harabuchi, M. Hatanaka, and S. Maeda, *Chem. Phys. Lett.* **737**, 100007 (2019).
- <sup>7</sup>M. E. Casida, K. C. Casida, and D. R. Salahub, *Int. J. Quantum Chem.* **70**, 933 (1998).
- <sup>8</sup>B. Patrizi, C. Cozza, A. Pietropaolo, P. Foggi, and M. Siciliani de Cumis, *Molecules* **25**, 430 (2020).
- <sup>9</sup>N. T. Maitra, F. Zhang, R. J. Cave, and K. Burke, *J. Chem. Phys.* **120**, 5932 (2004).
- <sup>10</sup>P. Elliott, S. Goldson, C. Canahui, and N. T. Maitra, *Chem. Phys.* **391**, 110 (2011).
- <sup>11</sup>M. J. Allen and D. J. Tozer, *J. Chem. Phys.* **113**, 5185 (2000).
- <sup>12</sup>D. J. Tozer, R. D. Amos, N. C. Handy, B. O. Roos, and L. Serrano-Andrés, *Mol. Phys.* **97**, 859 (1999).
- <sup>13</sup>A. Dreuw and M. Head-Gordon, *J. Am. Chem. Soc.* **126**, 4007 (2004).
- <sup>14</sup>P.-F. Loos, A. Scemama, and D. Jacquemin, *J. Phys. Chem. Lett.* **11**, 2374 (2020).
- <sup>15</sup>D. Jacquemin, V. Wathelet, E. A. Perpète, and C. Adamo, *J. Chem. Theory Comput.* **5**, 2420 (2009).
- <sup>16</sup>A. D. Laurent and D. Jacquemin, *Int. J. Quantum Chem.* **113**, 2019 (2013).
- <sup>17</sup>T. M. Maier, H. Bahmann, A. V. Arbuznikov, and M. Kaupp, *J. Chem. Phys.* **144**, 074106 (2016).
- <sup>18</sup>D. López-Carballera and T. Polcar, *Diamond Relat. Mater.* **108**, 107959 (2020).
- <sup>19</sup>J. Liang, X. Feng, D. Hait, and M. Head-Gordon, *J. Chem. Theory Comput.* **18**, 3460 (2022).
- <sup>20</sup>A. Ipatov, A. Fouqueau, C. P. del Valle, F. Cordova, M. E. Casida, A. M. Köster, A. Vela, and C. J. Jamorski, *J. Mol. Struct.: THEOCHEM* **762**, 179 (2006).
- <sup>21</sup>J. Carmona-Espíndola and A. M. Köster, *Can. J. Chem.* **91**, 795 (2013).
- <sup>22</sup>A. M. Köster, *J. Chem. Phys.* **118**, 9943 (2003).
- <sup>23</sup>A. Alvarez-Ibarra and A. M. Köster, *J. Chem. Phys.* **139**, 024102 (2013).

- <sup>24</sup>J. N. Pedroza-Montero, J. L. Morales, G. Geudtner, A. Álvarez-Ibarra, P. Calaminici, and A. M. Köster, *J. Chem. Theory Comput.* **16**, 2965 (2020).
- <sup>25</sup>D. Mejía-Rodríguez, R. I. Delgado Venegas, P. Calaminici, and A. M. Köster, *J. Chem. Theory Comput.* **11**, 1493 (2015).
- <sup>26</sup>J. Carmona-Espíndola, R. Flores-Moreno, and A. M. Köster, *J. Chem. Phys.* **133**, 084102 (2010).
- <sup>27</sup>L. D. Landau and E. M. Lifshitz, *Quantum Mechanics. Non-Relativistic Theory* (Pergamon Press, 1977), Vol. III.
- <sup>28</sup>S. P. Karna and M. Dupuis, *J. Comput. Chem.* **12**, 487 (1991).
- <sup>29</sup>F. A. Delesma, R. I. Delgado-Venegas, D. R. Salahub, J. M. del Campo, J. N. Pedroza-Montero, P. Calaminici, and A. M. Köster, *J. Chem. Theory Comput.* **17**, 6934 (2021).
- <sup>30</sup>D. Mejía-Rodríguez and S. B. Trickey, *Theor. Chem. Acc.* **140**, 37 (2021).
- <sup>31</sup>M. E. Casida, in *Recent Advances in Density Functional Methods (Part I)*, edited by D. P. Chong (World Scientific, 1995), pp. 155–192.
- <sup>32</sup>S. Hirata and M. Head-Gordon, *Chem. Phys. Lett.* **314**, 291 (1999).
- <sup>33</sup>P. A. M. Dirac, *Math. Proc. Cambridge Philos. Soc.* **26**, 376 (1930).
- <sup>34</sup>S. H. Vosko, L. Wilk, and M. Nusair, *Can. J. Phys.* **58**, 1200 (1980).
- <sup>35</sup>T. H. Dunning, *J. Chem. Phys.* **90**, 1007 (1989).
- <sup>36</sup>P. Calaminici, F. Janetzko, A. M. Köster, R. Mejía-Olvera, and B. Zuniga-Gutierrez, *J. Chem. Phys.* **126**, 044108 (2007).
- <sup>37</sup>N. Godbout, D. R. Salahub, J. Andzelm, and E. Wimmer, *Can. J. Chem.* **70**, 560 (1992).
- <sup>38</sup>D. Rocca, M. Vörös, A. Gali, and G. Galli, *J. Chem. Theory Comput.* **10**, 3290 (2014).
- <sup>39</sup>J. Berkowitz, *Photoabsorption, Photoionization, and Photoelectron Spectroscopy* (Elsevier, 1979), pp. 35–72.
- <sup>40</sup>A. M. Koster, G. Geudtner, A. Alvarez-Ibarra, P. Calaminici, M. E. Casida, J. Carmona-Espíndola, V. D. Dominguez, R. Flores-Moreno, G. U. Gamboa, A. Goursot, T. Heine, A. Ipatov, A. de la Lande, F. Janetzko, J. M. del Campo, D. Mejía-Rodriguez, J. U. Reveles, J. Vasquez-Perez, A. Vela, B. Zuniga-Gutierrez, and D. R. Salahub, eMon2k, Version 6, The deMon developers, Cinvestav, Mexico City (2018).
- <sup>41</sup>E. Aprà, E. J. Bylaska, W. A. de Jong, N. Govind, K. Kowalski, T. P. Straatsma, M. Valiev, H. J. J. van Dam, Y. Alexeev, J. Anchell, V. Anisimov, F. W. Aquino, R. Atta-Fynn, J. Autschbach, N. P. Bauman, J. C. Becca, D. E. Bernholdt, K. Bhaskaran-Nair, S. Bogatko, P. Borowski, J. Boschen, J. Brabec, A. Bruner, E. Cauët, Y. Chen, G. N. Chuev, C. J. Cramer, J. Daily, M. J. O. Deegan, T. H. Dunning, M. Dupuis, K. G. Dyall, G. I. Fann, S. A. Fischer, A. Fonari, H. Frücht, L. Gagliardi, J. Garza, N. Gawande, S. Ghosh, K. Glaesemann, A. W. Götz, J. Hammond, V. Helms, E. D. Hermes, K. Hirao, S. Hirata, M. Jacquelein, L. Jensen, B. G. Johnson, H. Jónsson, R. A. Kendall, M. Klemm, R. Kobayashi, V. Konkov, S. Krishnamoorthy, M. Krishnan, Z. Lin, R. D. Lins, R. J. Littlefield, A. J. Logsdail, K. Lopata, W. Ma, A. V. Marenich, J. Martin del Campo, D. Mejía-Rodriguez, J. E. Moore, J. M. Mullin, T. Nakajima, D. R. Nascimento, J. A. Nichols, P. J. Nichols, J. Nieplocha, A. Otero-de-la-Roza, B. Palmer, A. Panyala, T. Pirojsirikul, B. Peng, R. Peverati, J. Pittner, L. Pollack, R. M. Richard, P. Sadayappan, G. C. Schatz, W. A. Shelton, D. W. Silverstein, D. M. A. Smith, T. A. Soares, D. Song, M. Swart, H. L. Taylor, G. S. Thomas, V. Tipparaju, D. G. Truhlar, K. Tsemekhman, T. Van Voorhis, Á. Vázquez-Mayagoitia, P. Verma, O. Villa, A. Vishnu, K. D. Vogiatzis, D. Wang, J. H. Weare, M. J. Williamson, T. L. Windus, K. Wolinski, A. T. Wong, Q. Wu, C. Yang, Q. Yu, M. Zacharias, Z. Zhang, Y. Zhao, and R. J. Harrison, *J. Chem. Phys.* **152**, 184102 (2020).
- <sup>42</sup>E. R. Davidson, *J. Comput. Phys.* **17**, 87 (1975).
- <sup>43</sup>M. J. G. Peach, P. Benfield, T. Helgaker, and D. J. Tozer, *J. Chem. Phys.* **128**, 044118 (2008).
- <sup>44</sup>M. Schreiber, M. R. Silva-Junior, S. P. A. Sauer, and W. Thiel, *J. Chem. Phys.* **128**, 134110 (2008).
- <sup>45</sup>P.-F. Loos, A. Scemama, A. Blondel, Y. Garniron, M. Caffarel, and D. Jacquemin, *J. Chem. Theory Comput.* **14**, 4360 (2018).
- <sup>46</sup>P.-F. Loos, F. Lipparini, M. Boggio-Pasqua, A. Scemama, and D. Jacquemin, *J. Chem. Theory Comput.* **16**, 1711 (2020).
- <sup>47</sup>J. P. Perdew, K. Burke, and M. Ernzerhof, *Phys. Rev. Lett.* **77**, 3865 (1996).
- <sup>48</sup>A. D. Becke, *Phys. Rev. A* **38**, 3098 (1988).
- <sup>49</sup>J. P. Perdew, *Phys. Rev. B* **33**, 8822 (1986).
- <sup>50</sup>J. Carmona-Espíndola, J. L. Gázquez, A. Vela, and S. B. Trickey, *J. Chem. Phys.* **142**, 054105 (2015).
- <sup>51</sup>J. Carmona-Espíndola, J. L. Gázquez, A. Vela, and S. B. Trickey, *J. Chem. Theory Comput.* **15**, 303 (2019).
- <sup>52</sup>S. E. Pérez-Figueredo, P. Calaminici, and A. M. Köster, *J. Phys. Chem. A* **123**, 4565 (2019).
- <sup>53</sup>B. Doser, D. S. Lambrecht, J. Kussmann, and C. Ochsenfeld, *J. Chem. Phys.* **130**, 064107 (2009).
- <sup>54</sup>S. Nosé, *J. Chem. Phys.* **81**, 511 (1984).
- <sup>55</sup>W. G. Hoover, *Phys. Rev. A* **31**, 1695 (1985).
- <sup>56</sup>G. J. Martyna, M. L. Klein, and M. Tuckerman, *J. Chem. Phys.* **97**, 2635 (1992).
- <sup>57</sup>M. Moseler, H. Häkkinen, and U. Landman, *Phys. Rev. Lett.* **87**, 053401 (2001).
- <sup>58</sup>Y. Shao, Y. Mei, D. Sundholm, and V. R. I. Kaila, *J. Chem. Theory Comput.* **16**, 587 (2020).
- <sup>59</sup>M. J. G. Peach and D. J. Tozer, *J. Phys. Chem. A* **116**, 9783 (2012).
- <sup>60</sup>M. R. Silva-Junior, M. Schreiber, S. P. A. Sauer, and W. Thiel, *J. Chem. Phys.* **129**, 104103 (2008).
- <sup>61</sup>E. E. Rennie, C. A. F. Johnson, J. E. Parker, D. M. P. Holland, D. A. Shaw, and M. A. Hayes, *Chem. Phys.* **229**, 107 (1998).
- <sup>62</sup>J. M. Gingell, *Faraday Discuss.* **109**, 361 (1998).
- <sup>63</sup>C. Joblin, A. Leger, and P. Martin, *Astrophys. J.* **393**, L79 (1992).
- <sup>64</sup>A. Baiardi, L. Paoloni, V. Barone, V. G. Zakrzewski, and J. V. Ortiz, *J. Chem. Theory Comput.* **13**, 3120 (2017).
- <sup>65</sup>I. Benkyi, E. Tapavicza, H. Fliegl, and D. Sundholm, *Phys. Chem. Chem. Phys.* **21**, 21094 (2019).